ChemComm

COMMUNICATION

View Article Online
View Journal | View Issue

Cite this: *Chem. Commun.*, 2022, **58**, 6906

Received 28th February 2022,
Accepted 26th May 2022

DOI: 10.1039/d2cc01226j

rsc.li/chemcomm

Mechanistic insights of molecular metal polyselenides for catalytic hydrogen generation†

Alexander Elliott, ‡[a] James McAllister,‡[a] Liudvika Masaityte, [a] Mireia Segado-Centellas,[b] De-Liang Long, [a] Alexey Y. Ganin, [a] Yu-Fei Song, *[c] Carles Bo*[b] and Haralampos N. Miras *[a]

Molecular metal chalcogenides have attracted great attention as electrocatalysts for the hydrogen evolution reaction (HER). However, efficient utilisation of the active sites and catalytic performance modulation has been challenging. Here we explore the design of immobilized molecular molybdenum polyselenides $[Mo_2O_2S_2(Se_2)(Se_x)]^{2-}$ that exhibit efficient hydrogen evolution at low overpotential and stability over 1000 cycles. Density functional calculations provide evidence of a unimolecular mechanism in the HER process *via* the exploration of viable reaction pathways. The discussed findings are of a broad interest in the development of efficient molecular electrocatalytic materials.

Development of catalysts for the hydrogen evolution reaction (HER) is one of the key challenges in the realisation of a hydrogen economy based on electrocatalytic water splitting. The best performing HER catalyst is platinum, however its high cost and low natural abundance makes the development of noble-metal free catalysts an important area of research.[1] A variety of transition metal chalcogenides (ME_x) (M = Co, Fe, Ni, V, Nb, Ta, Mo, W; E = S, Se, Te) have been explored[2–9] in a quest for discovery of low production cost catalysts with high catalytic activity, and stability under aqueous corrosive conditions. Despite the extensive research conducted in this area, even the well explored chalcogenide, MoS_2[9–11] significantly underperforms as electrocatalyst for HER compared to Pt. This is due to the fact that most of the activity in MoS_2 comes from the edge sites which represent only a small fraction of the overall number of active sites in solid state materials like MoS_2. Interestingly, molecular oxochalcogenides can incorporate by design a significant number of functional groups (which mimic very effectively the edge of solid-state chalcogenides) and have been shown to be at least as stable and effective as solid-state analogues. For example, the $[Mo_2^{V}(S_2)_6]^{2-}$ cluster contains three disulphides per molybdenum,[12] while the hybrid family of $LMo^{VI}O(S_2)_2$ (where L = bidentate ligand) type catalysts exhibited an indicative cooperative electronic effect between the inorganic and organic components.[13–15] When immobilised on an appropriate surface, they can effectively act as heterogeneous catalysts. Additionally, the design of the catalyst's key components (*e.g.* metal centres, type and number of chalcogens) can be pre-determined using a precise molecular chemistry approach. The all-inorganic molybdenum- and tungsten-based sulphide catalysts has shown overpotentials as low as -114 ± 3 mV at 10 mA cm^{-2}.[16] The presence of well-defined molecular structures rendered the computational modelling more informative and reinforced our understanding of the HER mechanism. Theoretical calculations demonstrated that the reduction occurs on the disulphide ligand, while the terminal oxo ligand stabilise the negative charge developed during the catalytic process. Interestingly, investigation of other molecular chalcoxide equivalents[17–20] for the HER and exploration of the edge based catalytic sites has not previously been attempted.

In this work, we investigated the effects of stoichiometric and structural control resulting from the appropriate combination of chalcogen elements and their ratio (*e.g.* O^{2-}/Se_2^{2-}) within the coordination sphere of earth abundant transition metals and compare their mechanistic differences with their sulfur analogues.

The dimeric nanocluster, $[Mo_2O_2(\mu\text{-}Se)_2(Se_2)(Se_2)]^{2-}$ **1**, was synthesised following a facile method under mild conditions. The synthetic approach exploits the selenophilicity of molybdenum by exposing an alkaline molybdate solution to selenizing conditions. Alternatively, at elevated temperature and pressure regimes, the equilibrium shifts towards the formation of a mixture of species with the general formulae $[Mo_2O_2(\mu\text{-}Se)_2(Se_2)(Se_x)]^{2-}$ (where $x = 2$–4) **2**.

[a] *School of Chemistry, The University of Glasgow, Glasgow G12 8QQ, UK. E-mail: charalampos.moiras@glasgow.ac.uk*
[b] *Institute of Chemical Research of Catalonia (ICIQ), The Barcelona Institute of Science and Technology, Avgda. Països Catalans 16, 43007 Tarragona, Spain. E-mail: cbo@iciq.cat*
[c] *State Key Laboratory of Chemical Resource Engineering, Beijing Advanced Innovation Center for Soft Matter Science and Engineering, Beijing University of Chemical Technology, Beijing 100029, China. E-mail: songyf@mail.buct.edu.cn*

† Electronic supplementary information (ESI) available: The experimental method, materials characterization, electrochemical data and calculation method. CCDC 2155514 (**1**) and 2155450 (**2**). For ESI and crystallographic data in CIF or other electronic format see DOI: https://doi.org/10.1039/d2cc01226j

‡ These authors contributed equally.

During the reaction the species $[Mo_2O_2(\mu\text{-}Se)_2(Se_2)(Se_2)]^{2-}$, $[Mo_2O_2(\mu\text{-}Se)_2(Se_2)(Se_3)]^{2-}$ and $[Mo_2O_2(\mu\text{-}Se)_2(Se_2)(Se_4)]^{2-}$, seem to be in an equilibrium under harsh experimental conditions and found to co-crystallise within the same unit cell. Each method yielded orange-red crystals which were characterized by single crystal and powder X-ray structural analysis, FT-IR, ^{77}Se NMR and high-resolution electrospray ionization mass spectroscopy (ESI-MS). Subsequently, the $[Mo_2O_2(\mu\text{-}Se)_2(Se_2)_2]^{2-}$ **1** species was investigated as potential electrocatalyst to produce H_2 gas from acidic media where was found to exhibit excellent activity towards the hydrogen evolution reaction (HER). The oxoselenometalate compounds were synthesized under nitrogen atmosphere, following an optimised facile two-step process (see ESI†) utilizing low-cost materials, thus illustrating their potential for economically viable scalability.

The facile two-step synthetic procedure yields orange-red crystals and their single crystal X-ray diffraction (XRD) analysis shows that $[(CH_3)_4N]_2[Mo_2O_2(\mu\text{-}Se)_2(Se_2)_2]$ **1** crystallises in the orthorhombic system space group $Pca2_1$ with unit cell dimensions of a = 18.614(10), b = 11.422(6), c = 11.422(6) Å. The powder X-ray diffraction study conducted on the freshly synthesised material **1** (Fig. S5, ESI†) further confirm the purity of the synthesised material in the hexa-selenide form. Alternatively, the more challenging high temperature and pressure synthesis gives crystals containing a mixture of seleno-containing species with the formula $[(CH_3)_4N]_2[Mo_2O_2(\mu\text{-}Se)_2(Se_2)_2]_{0.25}[Mo_2O_2(\mu\text{-}Se)_2(Se_2)(Se_3)]_{0.25}[Mo_2O_2(\mu\text{-}Se)_2(Se_2)\ (Se_4)]_{0.5}$ **2** which crystallises in the triclinic space group $P\bar{1}$ with unit cell dimensions of a = 10.098(4), b = 12.766(5), c = 18.713(7) Å, (α =78.432(4)°, β = 80.140(4)° and γ = 86.939(4)°). Fig. 1 displays the crystal structures of the $[Mo_2O_2(\mu\text{-}Se)_2(Se_2)_2]^{2-}$ **1** and the $[Mo_2O_2(\mu\text{-}Se)_2(Se_2)(Se_4)]^{2-}$ anion found in **2** respectively. The $[Mo_2O_2(\mu\text{-}Se)_2(Se_2)_2]^{2-}$ and $[Mo_2O_2(\mu\text{-}Se)_2(Se_2)(Se_4)]^{2-}$ anions are constructed by two molybdenum centres that are mutually linked by two $\mu\text{-}Se^{2-}$ bridges, and a Mo^V–Mo^V separation of 2.885(1) and 2.884(2) Å. In addition, the coordination sphere of each molybdenum centre is completed by a terminal oxo group of Mo=O bond distances 1.687(8) and 1.68(1) Å and two selenide bridging atoms with an average Mo–(μ-Se) bond distances of *ca.* 2.447 and 2.461 Å, respectively.

Finally, in the case of the $[Mo_2O_2(\mu\text{-}Se)_2(Se_2)_2]^{2-}$ anion the coordination sphere of Mo is completed by two terminal diselenide (Se_2^{2-}) groups with an average Se–Se bond distance of *ca.* 2.323 Å, while in the case of $[Mo_2O_2(\mu\text{-}Se)_2(Se_2)(Se_4)]^{2-}$ that is by a diselenide (Se_2^{2-}) and a tetraselenide (Se_4^{2-}) group with average Se–Se bond distance of *ca.* 2.333 Å. The overall charge of the compound is compensated by two tetramethylammonium, $(CH_3)_4N^+$, cations per dimeric cluster.

In an effort to further characterize the isolated compounds, we employed high resolution electrospray ionization mass spectrometry (ESI-MS)[21–23] to determine the composition of the oxoselenometalate species in solution. The ESI-MS studies were performed in CH_3CN. A series of singly charged distribution envelopes were observed, all in the region of 500–1000 *m*/*z* (Fig. S4, ESI†). More specifically, the distribution envelopes centred at 699.18 *m*/*z* value can be assigned to the intact compound $[Mo_2O_2(\mu\text{-}Se)_2(Se_2)_2]^{2-}$. Additionally, ^{77}Se NMR spectrum of **1** recorded in DMF. The spectrum shows two distinct peaks corresponding to the two unique environments in the dimer located at shifts of 134 and 711 ppm relative to Me_2Se (Fig. S6, ESI†).

To investigate the HER activity of the molecular catalyst we immobilised the catalyst on a glassy carbon electrode (GCE) support (see ESI†).

The amount of catalyst on the electrode surface was controlled by adjusting the loading concentration and volume. The performance of the catalyst improves as a function of the catalyst loading up to the value of 3.38 μmol cm^{-2}. Beyond this value the quality and mechanical stability of the produced electrocatalytic film degrades which leads either to similar or inferior performance due to detachment of the film from the electrode's surface. The results reported in Fig. 2 indicate that the cluster is highly active towards HER revealing a very small onset (40 mV) and low overpotential of −165 ± 3 mV (at j = 10 mA cm^{-2}) as a function of the catalyst loading. Consequently, further increase of the applied overpotential results in a rapid rise of the cathodic current, which is

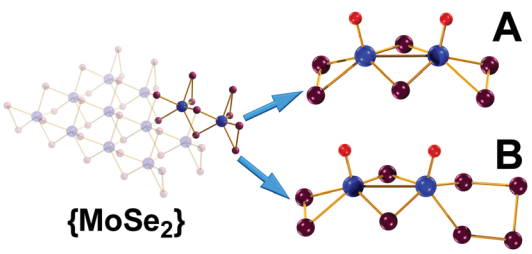

Fig. 1 Ball-and-stick representation of: (A) $[Mo_2O_2(\mu\text{-}Se)_2\ (Se_2)_2]^{2-}$ and (B) $[Mo_2O_2(\mu\text{-}Se)_2(Se_2)(Se_4)]^{2-}$. Colour code: Mo, Blue; Se, plum; O, red; Counterions are omitted for clarity.

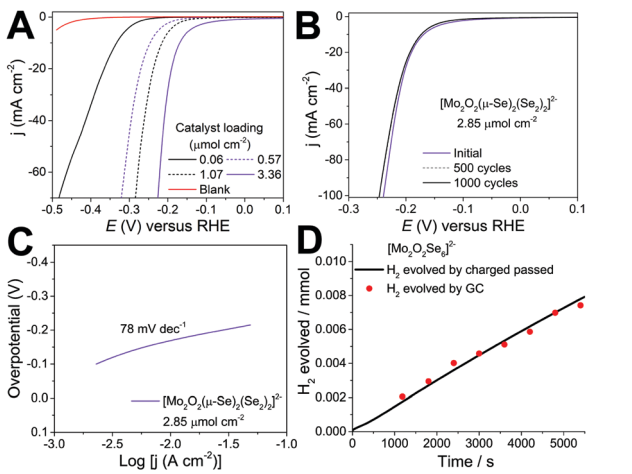

Fig. 2 Electrochemical measurements of the molecular chalcoxide for HER electrocatalysis in 1 M H_2SO_4. (A) Observed polarisation curves as a function of the concentration of the catalyst; (B) Stability of the catalyst after 1000 cycles; (C) Corresponding Tafel plot and (D) Hydrogen evolved over time determined by charge passed (black line) and gas chromatography (red squares) $(Me_4N)_2[Mo_2O_2(\mu\text{-}Se)_2(Se_2)_2]$ deposited on glassy carbon electrode.

indicative of HER activity, in marked contrast to the bare GCE with carbon powder.

An important prerequisite of functional components used for large scale applications *e.g.* electrochemical water-splitting devices is the durability of the materials used. To assess this, we employed potential cycling as a simulation of the start-up/shutdown conditions found in an electrolyser to provide us with information on the catalysts' long-term stability. Using catalyst **1** (3.38 μmol cm^{-2}), we applied an accelerated scan rate of 100 mV s^{-1} between a potential range of 0.10 to −0.25 V (vs RHE) for 1000 cycles, Fig. 2b. At the end of the cycling, the catalyst showed negligible loss in cathodic current density, reaching an impressive density of $j > 100$ mA cm^{-2} below 250 mV. These results attest to the electrochemical stability of $[Mo_2O_2(\mu\text{-}Se)_2(Se_2)_2]^{2-}$ **1** and its potential use in electrochemical HER devices. Finally, to confirm that the reaction taking place on the working electrode corresponds to the hydrogen evolution reaction (HER), the evolved gas was analysed using gas chromatography (Fig. S8, ESI†). As such, the faradaic efficiency of the molecular catalyst in 1 M H_2SO_4 was determined to be 102.3% ± 3.0 with a TOF of 0.019 s^{-1} at −190 mV demonstrating the evolution of hydrogen at full faradaic efficiency.

To investigate the underlying processes and reaction pathways, the electronic structure of these molecules and their reduced analogues were studied on the basis of density functional theory (DFT). The geometries of both anions were optimised starting from the single crystal X-ray diffraction data (see ESI†). The electronic structure of these anions is similar and according to orbital analysis and charge distribution, both ligands – bidentate $\kappa^{1,4}$-Se_4^{2-} and side on η^2-Se_2^{2-} – formally contribute −2 charges each. Mo centres present +5 formal oxidation state with a Mo–Mo bond (2.855 Å) as corroborated by the bond valence sum calculations analyses and the crystal structure. Each perselenide moiety has a doubly filled $\pi^{*2}\pi^{*2}$ group molecular orbital (MO) pair.

Examination of the HOMO–LUMO gap provides a preliminary good estimation of the chemical potential of the species and indication of orbitals populated by the incoming electrons. 0 e^- and 1 e^- reduction of catalytic species are depicted in Fig. S9 (ESI†). In case of 0 e^-, the energy gap is higher in $[Mo_2O_2(\mu\text{-}Se)_2(Se_2)_2]^{2-}$ than $[Mo_2O_2(\mu\text{-}Se)_2(Se_2)(Se_4)]^{2-}$ and follows the same trend as sulphur analogues of these compounds. However, the HOMO–LUMO gap and LUMO energy are smaller in selenium analogues compared to their respective sulphur anions (Fig. S9 and S10, ESI†). The first unoccupied MOs involve d metallic orbitals and a σ-antibonding Se–Se orbital. Interestingly, in case of 1 e^- reduced species, the energy needed to insert the second electron is higher for Se compounds than S analogues (Fig. S9 and S10, ESI†). The half occupied orbital present Sigma Se–Se antibonding character. In order to investigate the electrochemical steps that are taking place it is important to identify the different pathways following the two-fold reduction of the molecular catalysts leading to protonation equilibria. Therefore, the stability of all possible isomeric forms was evaluated. Even though those unprotonated and short-lived species may not be detected and characterised in solution, evaluating their relevant stability is relevant as it can serve as a reference state for subsequent steps.

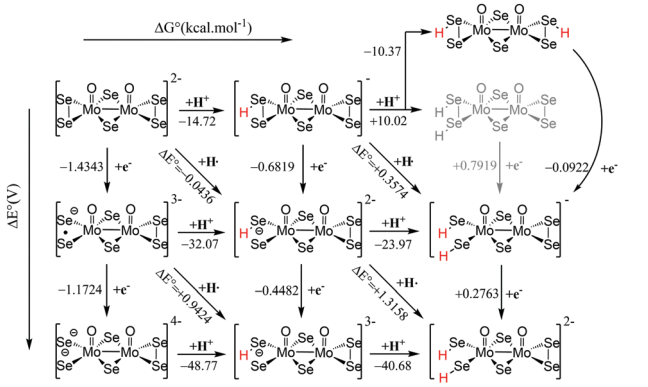

Fig. 3 Thermodynamic routes for compound $[Mo_2O_2(\mu\text{-}Se)_2(Se_2)_2]^{2-}$ **1** with two variables: electron addition (vertical) and proton addition (horizontal).

Considering the symmetric structure of the $[Mo_2O_2(\mu\text{-}Se)_2(Se_2)_2]^{2-}$ complex, we explored a series of isomers that can be formed during the two-variable proton/electron addition leading to the global panorama of possible HER equilibria (Fig. 3). The cleavage of perselenide bond upon 1 e^- and 2 e^- reduction was observed. It is expected based on molecular orbital analysis, because these anions feature σ-antibonding Se–Se orbitals which might in principle be occupied by incoming electrons inducing the breaking of Se–Se bond. This behaviour was also observed in the sulphur analogues of these anions. The complete nomenclature of the obtained isomers and proton affinities are listed in the Fig. S12–S19 (ESI†). For compound **1**, the most stable doubly reduced and single-protonated species is B1 since it stabilises the mitigation of charge developed in the newly formed diselenol species. Consequently, the second protonation step which derives from B1 is BB1, which exhibits a free energy value of −40.7 kcal mol^{-1} (see Fig. S12, ESI†). Taking into consideration the proximity of the neighbouring hydrogen atoms in this structure, that raised the possibility of the existence of a Tafel-type re-combination step. Further examination of this step for both anions revealed activation energies of 62 kcal mol^{-1} from double-protonated BB1 (Fig. S21 and S26, ESI†) which are too high to be operative at room temperature. To this extend, departing from BA1 whereas one selenium and one oxygen atom are protonated, Taffel reaction activation energy is more favourable with an activation energy of 37.45 kcal mol^{-1} (Fig. S22, ESI†). In a similar manner, we aimed to examine the Heyrovsky step departing from single- and double-protonated $[H_2Mo_2O_2(\mu\text{-}Se)_2(Se_2)(Se_x)]^{2-}$ (x = 2, 4) structures. This step is thermodynamically favourable across the range of molecular systems with calculated released energies within −46.12 to −4.51 kcal mol^{-1} (Fig. 4 and Fig. S20, S23–S25, ESI†). The activation energy for this step is in range of +2.54 to +18.62 kcal mol^{-1} for both anions and all reactant complexes taken into consideration. These E_a values indicate that activation can happen at room temperature conditions. For compound **1**, BB1 intermediate $[H_2Mo_2O_2(\mu\text{-}Se)_2(Se_2)_2]^{2-}$, the obtained transition state has a relative free energy value $\Delta G^{\ddagger}$ = +18.62 kcal mol^{-1} (Fig. S20, ESI†) which is comparable to the activation energy value obtained for compound **2** when the protons interact with the side on η^2-Se_2^{2-} terminal group

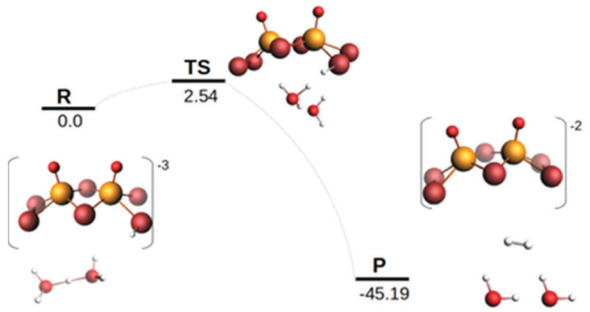

Fig. 4 Activation energy and transition state for **B1** $H[Mo_2O_2(\mu\text{-}Se)_2(Se_2)_2]^{3-}$.

(BB1, Fig. S24, ESI,† $\Delta G^{\ddagger}$ = +16.52 kcal mol^{-1}). Interestingly, when the interaction takes place on the bidentate $\kappa^{1,4}$-Se_4^{2-} terminal site the calculated activation energy and transition state for $[H_2Mo_2O_2(\mu\text{-}Se)_2(Se_2)(Se_4)]^{2-}$ (BB3) was found to be lower ($\Delta G^{\ddagger}$ = +14.4 kcal mol^{-1} (Fig. S25, ESI†).

It is worth noting that single-protonated forms have significantly lower activation energies than the double-protonated ones. The activation barriers for compounds **1** (B1) and **2** are only 2.54 (Fig. 4) and 5.18 kcal mol^{-1} (Fig. S23, ESI†), respectively. Thus, the model of the transition state for single protonated forms is the most probable candidate. For the non-reduced, single- and double-reduced species, their double-protonated forms are the most thermodynamically stable. Considering electrochemical routes, 2e$^-$ addition to double-protonated non-reduced species is non-favourable. In contrast, reduction reactions from single protonated and non-protonated forms are more feasible (Fig. 3). Thus, our results clearly point towards the Heyrovsky mechanism based on thermodynamic favourability and the high activation energies observed for the alternative Taffel step.

In conclusion, a more accessible and high-yield synthesis for the selenium analogue to the well-known $[Mo_2O_2S_2(S_2)_2]^{2-}$ structure makes it possible to explore the electronic and chemical properties of the molecule, which have previously remained unexplored. The performance of the molecular catalyst for the hydrogen evolution reaction was evaluated while we propose viable mechanistic pathways in relation to the interaction between catalysts and substrate while we identified intriguing differences with their sulfur analogues. The initial 1 e$^-$ reduction is easier compared to the sulphur containing analogue however the second reduction is more energetically demanding which is reflected to the observed slightly elevated Tafel slope. This indicates the significant electronic changes of the selenium containing structure relative to the sulphur. Notably, these results represent an attractive strategy for preparing next generation HER electrocatalysts. Understanding the electronic underpinnings of trends in activity as a function of the metal or chalcogen incorporated in the molecular species, can help inform the design of new catalysts and exploitation of cooperative and structural effects. Moreover, the development of facile low-cost synthesis of a molecular catalyst is highly desirable for the easier scale up in large scale applications.

Conflicts of interest

There are no conflicts to declare.

Notes and references

1 X. Zou and Y. Zhang, *Chem. Soc. Rev.*, 2015, **44**, 5148–5180.
2 J. C. McGlynn, T. Dankwort, L. Kienle, N. A.-G. Bandeira, J. P. Fraser, E. K. Gibson, I. Cascallana-Matías, K. Kamarás, M. D. Symes, H. N. Miras and A. Y. Ganin, *Nat. Commun.*, 2019, **10**, 4916.
3 L. Najafi, S. Bellani, R. Oropesa-Nuñez, B. Martín-García, M. Prato, L. Pasquale, J.-K. Panda, P. Marvan, Z. Sofer and F. Bonaccorso, *ACS Catal.*, 2020, **10**, 3313–3325.
4 J. C. McGlynn, M. Friskey and A. Y. Ganin, *Sustainable Energy Fuels*, 2020, **4**, 4473–4477.
5 J. Yang, A. R. Mohmad, Y. Wang, R. Fullon, X. Song, F. Zhao, I. Bozkurt, M. Augustin, E. J.-G. Santos, H. S. Shin, W. Zhang, D. Voiry, H. Y. Jeong and M. Chhowalla, *Nat. Mater.*, 2019, **18**, 1309–1314.
6 H. Kwon, D. Bae, H. Jun, B. Ji, D. Won, J.-H. Lee, Y.-W. Son, H. Yang and S. Cho, *Appl. Sci.*, 2020, **10**, 3087.
7 J. Shi, Y. Huan, X. Zhao, P. Yang, M. Hong, C. Xie, S. Pennycook and Y. Zhang, *ACS Nano*, 2021, **15**, 1858–1868.
8 A. S. Goloveshkin, N. D. Lenenko, A. V. Naumkin, A. Y. Pereyaslavtsev, A. V. Grigorieva, A. V. Shapovalov, V. N. Talanova, A. V. Polezhaev, V. I. Zaikovskii, V. V. Novikov, A. A. Korlyukov and A. S. Golub, *ChemNanoMat*, 2021, **7**, 447–456.
9 T. F. Jaramillo, K. P. Jørgensen, J. Bonde, J. H. Nielsen, S. Horch and I. Chorkendorff, *Science*, 2007, **317**, 100–102.
10 Q. Ding, B. Song, P. Xu and S. Jin, *Chem*, 2016, **1**, 699–726.
11 P. D. Tran, T. V. Tran, M. Orio, S. Torelli, Q. D. Truong, K. Nayuki, Y. Sasaki, S. Y. Chiam, R. Yi, I. Honma, J. Barber and V. Artero, *Nat. Mater.*, 2016, **15**, 640–646.
12 Z. Huang, W. Luo, L. Ma, M. Yu, X. Ren, M. He, S. Polen, K. Click, B. Garrett, J. Lu, K. Amine, C. Hadad, W. Chen, A. Asthagiri and Y. Wu, *Angew. Chem., Int. Ed.*, 2015, **54**, 15181–15185.
13 B. R. Garrett, S. M. Polen, K. A. Click, M. He, Z. Huang, C. M. Hadad and Y. Wu, *Inorg. Chem.*, 2016, **55**, 3960–3966.
14 B. R. Garrett, K. A. Click, C. B. Durr, C. M. Hadad and Y. Wu, *J. Am. Chem. Soc.*, 2016, **138**, 13726–13731.
15 B. R. Garrett, S. M. Polen, M. Pimplikar, C. M. Hadad and Y. Wu, *J. Am. Chem. Soc.*, 2017, **139**, 4342–4345.
16 J. McAllister, N. A.-G. Bandeira, J. C. McGlynn, A. Y. Ganin, Y.-F. Song, C. Bo and H. N. Miras, *Nat. Commun.*, 2019, **10**, 370.
17 J. H. Liao, L. Hill and M. G. Kanatzidis, *Inorg. Chem.*, 1993, **32**, 4650–4652.
18 C. nin Chau, R. W.-M. Wardle and J. A. Ibers, *Inorg. Chem.*, 1987, **26**, 2740–2741.
19 B. W. Eichhorn, D. R. Gardner, A. Nichols-Ziebarth, K. J. Ahmed and S. G. Bott, *Inorg. Chem.*, 1993, **32**, 5412–5414.
20 G.-C. Guo and T. C.-W. Mak, *Inorg. Chem.*, 1998, **37**, 6538–6540.
21 H. N. Miras, E. F. Wilson and L. Cronin, *Chem. Commun.*, 2009, 1297–1311.
22 H. N. Miras, M. Sorus, J. Hawkett, D. O. Sells, E. J.-L. McInnes and L. Cronin, *J. Am. Chem. Soc.*, 2012, **134**, 6980–6983.
23 J. Yan, D.-L. Long, H. N. Miras and L. Cronin, *Inorg. Chem.*, 2010, **49**, 1819–1825.